Part 2: Simulation Methodology and Numerical Uncertainty for RANS-CFD for the Hydrodynamics of Wind-Assisted Ships Operating at Leeway Angles

N.J. van der Kolk[1], I Akkerman, J.A. Keuning and R.H.M. Huijsmans

Ship Hydromechanics, Delft University of Technology, Mekelweg 2, 2628 CD, Delft, The Netherlands

***Abstract*:** A Reynolds-averaged Navier Stokes computational fluid dynamics (RANS-CFD) package will be one of the primary tools used during the development of a performance prediction program for wind-assisted commercial ships. The predominance of large-scale separated flow structures in the wake of the sailing ship, an artefact of sideforce production necessary for sailing, points to a careful estimate for the numerical uncertainty. This paper describes the simulation verification exercise, performed in support of the experimental validation presented in Part 1 of this two-part series describing the RANS-CFD method employed in this research. Methods for CFD uncertainty quantification are defined and implemented for verification cases at leeway angles equal to 0°, 6°, and 9°. Analysis for four sets of grids with different meshing strategies and for varying time steps results in a grid definition and time step for simulation validation. Numerical uncertainty as adopted in Part 1 for validation is defined. Finally, the full-scale simulation methodology, as used for the production runs of the Delft Wind Assist Series, is described.

Keywords: Numerical error; RANS; Computational fluid dynamics; Sailing vessels; Emission control areas; Green shipping

1 INTRODUCTION

Wind energy as an auxiliary form of propulsion for commercial ships has again become of great interest as a possible response to volatile fuel prices and increasingly stringent environmental regulations. As hybrid vessels, the performance of a wind-assist concept will depend on the contribution of the wind propulsor, alongside the efficiency of the conventional propulsion system and the drag penalty associated with heel and leeway: the “sailing condition”. Of course, the introduction of a sail-plan will only benefit the vessel if the net thrust gained outweighs any loss in main propulsor efficiency or increase in resistance. Also, the manoeuvrability of the vessel may be compromised. The expansion and refinement of regression-based modelling for a generic wind-assist vessel is the subject of ongoing work at Delft University of Technology.

The maturity of Reynolds-averaged Navier Stokes computational fluid dynamics (RANS-CFD) solvers offers the ready, inexpensive analysis for a large number of hull

[1] Corresponding author. E-mail: n.j.vanderkolk@tudelft.nl, Tel.: +31 (0)152788729

© 2020. This manuscript version is made available under the CC-BY-NC-ND 4.0 license https://creativecommons.org/licenses/by-nc-nd/4.0/. Published version: https://doi.org/10.1016/j.oceaneng.2020.107024

variations. However, simulations that remain computationally affordable may be unable to model the flow patterns occurring near a sailing commercial ship. Fluid flow around the wind-assisted ship operating at a leeway angle will experience separation effects and will become entrained in large vortices in the wake of the ship. Modeling the occurrence of separation and the evolution of these vortices is the principal simulation challenge, as both phenomena may challenge modeling assumptions made in the simulation setup.

The meshing strategy for simulation validation and for full-scale production runs is informed by a grid verification and parameter study, where numerical uncertainty is determined for several grid sets with differing meshing strategies, for a range of Courant numbers, and considering modeling choices such as wall treatment and turbulence models. It was observed that grids with a large refinement diffusion exhibited superior performance as measured by the calculated uncertainties. This is interpreted as a requirement on the refinement of the wake of the sailing vessel. The influence of cell size at the ship hull was most apparent for the sideforce uncertainty. Finally, improvement in geometric similarity for grid set Cnobl, defined without boundary layer cells, gave better-behaved convergence and resulted in lower uncertainty estimates. This implies that the uncertainty estimates for practical meshes (with boundary layer cells) may be overstated. A parameter study included modeling choices such as wall treatment and turbulence model selection, where an ensemble error, and simulation computation time was used to design the full-scale production runs.

This paper is Part 2 of a series describing the simulation method used during the study of the hydromechanics of wind-assist ships. An experimental validation of the simulation method was presented in Part 1. In this paper, a RANS-CFD methodology for computationally affordable assessment of large numbers of ship-hull variations. This simulation work is performed in the service of a regression-based modeling for the performance of wind-assist vessels. Production runs are performed with a six million cell grid, which gave numerical uncertainties that were commensurate with the uncertainties in the experimental data of the validation data (presented in Part 1 of this series. Finally, the meshing strategy adopted for full scale production runs is described, followed by a discussion of scale effects and validation level. Here, results for the sailing performance of hulls from the Delft Wind-assist Series are presented for simulations performed at model-scale and full-scale. The implications of simulation validation levels for the data reduction and derived quantities is also discussed. An effort is made to give physical explanation for the significant systematic differences.

2 METHODOLOGY

2.1 RANS-CFD Verification Procedure

A numerical simulation will have some error associated with discretization and an error associated with the iterative solution approach for the non-linear flow equations. The numeric error is written as the sum of discretization errors and iterative errors, with corresponding uncertainty, while disregarding round-off errors (Wilson, et al., 2006):

$$\delta_{\mathrm{Num}}^2 = \delta_{\mathrm{D}}^2 + \delta_{\mathrm{I}}^2 \quad \rightarrow \quad U_{\mathrm{Num}}^2 = U_{\mathrm{D}}^2 + U_{\mathrm{I}}^2 \qquad (1)$$

Several governing bodies publish standards for CFD simulation verification, including the International Towing Tank Committee (ITTC) and the American Society of Mechanical Engineers (ASME). The Grid Convergence Index (GCI) of Roache is commonly accepted, thanks in part to his strong advocacy for standardization of journal policies regarding uncertainty reporting for computational fluid dynamics. His influence is seen throughout subsequent work on this topic. The ITTC recommendations include the correction factor method of Stern and Wilson (Stern, et al., 2001), the GCI of Roache, and an approach for oscillatory convergence. Several methods are investigated in (van der Kolk, et al., 2016): the GCI of Roache (Roache, 1997), its elaboration by Eça and Hoekstra (Eça & Hoekstra, 2014), the Correction Factor of Stern (Stern, et al., 2001), and the Approximate Error Spline of Celik (Celik, et al., 2005). The method of Eça and Hoekstra was most robust for its ability to cope with nonconforming observed-order-of-convergence and otherwise anomalous convergence behaviour, and this method is followed for the discretization uncertainty for the remainder of this study. The iterative uncertainty is assessed by reviewing the normalized L2 residuals for the flow equations and the standard deviation for the integrated body forces used as verification quantities, presented in Section 2.3.

Most CFD verification procedures for discretization errors originate in the work of Richardson (Richardson, 1927), who identified the asymptotic approach to a continuum solution for finite difference calculations with increasing grid refinement. The so-called Richardson extrapolation was adopted by Roache (Roache, 1997) to estimate the uncertainty due to discretization errors in CFD. Beginning with the generalized Richardson extrapolation:

$$\phi_0 \cong \phi_1 + \frac{\phi_1 - \phi_2}{r^p - 1} \qquad (2)$$

$r = \frac{h_2}{h_1}$ is the grid refinement ratio for a characteristic grid height h. This is an expression for the function value at zero-grid spacing, based on the function value at a series of geometrically similar grids. For unsteady simulations, the time step has been scaled together with the grid spacing to achieve a constant Courant number for all grids. The exponent p is either the theoretical (second-order for space and time) or observed order of convergence. The observed order of convergence is calculated from a grid triplet as:

$$p_{Obs} = \ln\left(\frac{\phi_3 - \phi_2}{\phi_2 - \phi_1}\right) / \ln(r) \qquad (3)$$

The difference $\delta_{RE} = \phi_0 - \phi_1$ is an estimate of the error for grid one, corresponding to a 50% uncertainty band when this value is interpreted as a single realization of that error. Thus:

$$U_{50\%} = \delta_{RE} = \frac{\phi_1 - \phi_2}{r^p - 1} \qquad (4)$$

One might argue that δ_{RE} is derived from multiple realizations of the function: ϕ_1, ϕ_2, ϕ_3. Finally, to extend the confidence interval to 95% Roache defines the Grid Convergence Index (GCI) as:

$$GCI = F_s * |\delta_{RE}| \quad (5)$$

F_s is interpreted as the coverage factor or, in engineering parlance, as the factor of safety. Roache suggests $F_s = 3$ for rudimentary grid convergence studies involving two grids, and $F_s = 1.25$ for more rigorous studies.

The method is predicated on monotonic convergence behaviour for simulations with increasing mesh refinement or decreasing time step. The convergence ratio, R, must satisfy the following condition:

$$0 < R < 1 \quad (6)$$

$$R = \frac{\phi_2 - \phi_1}{\phi_3 - \phi_2} \quad (7)$$

This requirement leads to essential practical issues that complicate the application of Richardson extrapolation theory to RANS-CFD, chief among which is the definition of a family of systematically refined grids that lies within the asymptotic range and yet remains computationally feasible. Also problematic are limiters used in the discretization of the flow equations, modelling requirements for the 1st cell height at the ship hull, and non-conforming convergence rate where higher order terms in the power series expansion play a role.

The efforts of Roache have been carried further by Eça and Hoekstra (Eça & Hoekstra, 2014) (Eça, et al., 2010), who applied a least-squared approach to the determination of p_{Obs} to accommodate data scatter for the grid solution ϕ_i. Eça and Hoekstra also incorporate the error estimates with prescribed orders (Oberkampf, 1994), when data scatter is such that a reliable estimate for the order of convergence, p, is not feasible. In these cases, convergence is assumed to proceed with either first or second order, or with mixed order:

$$\delta_1 = c_1 h \quad (8)$$

$$\delta_2 = c_2 h^2 \quad (9)$$

$$\delta_{12} = c_1 h + c_2 h^2 \quad (10)$$

Also, recognizing that CFD for practical ship flows precludes the true approach to the asymptotic range while using systematically refined grids, Eça and Hoekstra propose a weighting within the least-squared minimization that favours the fine-grid solutions.

A selection is made among the available error estimates based on the observed order of convergence and the standard deviation for each fit for the solution on n grids. The extents of what is considered to be an expected value for p may be discussed, as the safety factor more than doubles at the boundary of this set. Eça and Hoekstra state that values of p_{obs} that fall between 0.6 and 2.1 may be treated with confidence, so that $F_s = 1.25$. For cases where p_{obs} is greater or less than the expected order of convergence, the power-series estimates with prescribed orders that best fits the data is selected, with an increased $F_s = 3$. Other researchers have questioned this substantial penalty for the uncertainty, especially for datasets that exhibit

monotonic convergence with an order that is near to two (Stern, et al., 2005) (Viola, et al., 2013).

$$\Delta_\phi = \frac{max(\phi) - min(\phi)}{n-1} \qquad (11)$$

When the error estimator has been selected, the uncertainty is determined by comparing the data range parameter, Δ_ϕ, with the standard deviation of the fit σ_{fit}.

$$\mathrm{U_{Eça}} = \begin{cases} F_s\delta_i + \sigma_{fit} + \left|\phi_i - \phi_{fit}\right| & \sigma_{fit} < \Delta_\phi \\ 3\sigma_{fit}/\Delta_\phi\left(F_s\delta_i + \sigma_{fit} + \left|\phi_i - \phi_{fit}\right|\right) & \sigma_{fit} \geq \Delta_\phi \end{cases} \qquad (12)\backslash$$

The first term may be recognized as the GCI of Roache. The remaining terms are the standard deviation of the fit and the difference between the data value ϕ_i, and the fit ϕ_{fit}. The ratio σ_{fit}/Δ_ϕ serves as metric for the quality of the data available for error estimation. For $\sigma_{fit}/\Delta_\phi \geq 1$, the factor of safety is increased in proportion to this ratio. A full description of this procedure is given in (Eça & Hoekstra, 2014).

2.2 Grid Set Definition

Simulation verification as described above requires a set of grids that are geometrically similar and cover a range of grid sizes within the asymptotic range. Geometric similitude is achieved in the simplest sense by progressive subdivision of mesh cells. For three-dimensional problems, the resulting grids may grow to exceed computing limits, so that a compromise is necessary according to the available computational power. Three grid sets were defined for this verification exercise, including one subset without boundary layer cells. Grid sets were defined to test the influence of cell distribution within the domain, the influence of refinement diffusion ratio, and the effect of grid similarity on the discretization uncertainty. Each set is composed of four grids, spanning approximately one complete subdivision of the coarse grid ($r = 2$).

An unstructured mesh for three-dimensional, complex geometries requires a definition for grid size. This dimension must be a length that is descriptive of the grid, and should decrease monotonically for a set of grids, preferably with constant refinement ratio r. Roache suggests the following:

$$h_{vol} = \sqrt[3]{\frac{vol}{N}} \qquad (13)$$

In which vol is the volume of the computational domain and N the number of cells. This definition for cell height is a global quantity: it does not reflect the distribution of cells throughout the domain according to the refinement diffusion, which is of particular importance for capturing flow structures around the hull. As a consequence of these ambiguities in the volumetric cell height metric h_{vol} defined in Equation 13, the observed order of convergence may not agree with the theoretical order of convergence. In other words,

a second-order discretization that is expected to converge with $(dx)^2$ may not behave accordingly with $(h_{vol})^2$

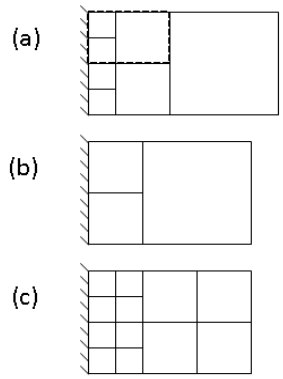


Figure 1 Illustration of the relationship between refinement level and refinement diffusion for mesh refinement.

Simulation verification as described above requires a set of grids that are geometrically similar and cover a range of grid sizes within the asymptotic range. Geometric similitude is achieved in the simplest sense by progressive subdivision of mesh cells. For three-dimensional problems, the resulting grids may grow to exceed computing limits, so that a compromise is necessary according to the available computational power.

The construction of a systematically refined set of unstructured grids using the Numeca meshing tool, Hexpress, is achieved by varying initial cell subdivision, which defines the cell size, and refinement diffusion, which defines the thickness of each refinement level, such that refinement diffusion doubles with each grid subdivision $(dx/2)$. In Figure 1, cells adjacent to a surface are given to illustrate these concepts. In Figure 2(a), the wall has a refinement level equal to two and a refinement diffusion equal to one. The size of the largest cell on the right is defined by the initial subdivision of the computational domain. That cell is refined twice in the vicinity of the wall, and each refinement level is one cell thick. Figure 2(b) is a detail of the cells adjacent to the wall. The refinement diffusion, or the thickness of each refinement level, is one. In 2(c), these cells have been divided once, so that $r = 2$. Here, the thickness of each refinement level is two, which is to say that the refinement diffusion has doubled.

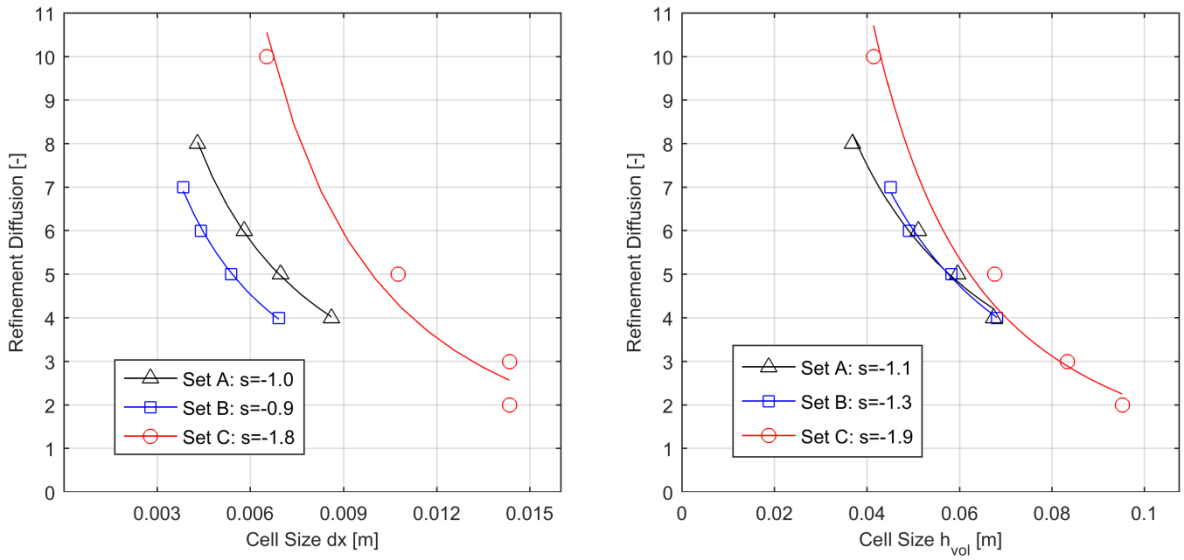


Figure 2 Definition of grid sets A, B, and C. The exponent in the curve fit for each set is provided in the legend as s.

Three grid sets were defined for this verification exercise, including one subset without boundary layer cells. Grid sets were defined to test the influence of cell distribution within the domain, the influence of refinement diffusion ratio, and the effect of grid similarity on the discretization uncertainty. Each set is composed of four grids, spanning approximately one complete subdivision of the coarse grid (r=2).

- Grid Set A - Higher refinement diffusion
- Grid Set B - Smaller cell size at hull
- Grid Set C - Twice diffusion rate
- Grid Set Cnobl - No boundary layers inserted

Table 1 Details of mesh construction.

Grid ID	Cell Count N	h_{vol}	h/h_1	BL Cells	Y^+ Mean (Max)	Courant Max (FS)
A4	2.0E+06	6.7E-02	1.83	5	56.5 (84)	3.9 (2.6)
A3	3.0E+06	6.0E-02	1.61	4	47.9 (75)	7.4 (4.2)
A2	4.7E+06	5.1E-02	1.38	3	47.9 (73)	6.0 (2.8)
A1	1.2E+07	3.7E-02	1.00	3	52.5 (80)	6.7 (3.3)
B4	2.0E+06	7.2E-02	1.51	4	54.4 (78)	7.5 (5.0)
B3	3.2E+06	6.1E-02	1.29	3	55.1 (79)	6.1 (4.3)
B2	5.3E+06	5.2E-02	1.09	3	53.8 (80)	5.3 (4.2)
B1	6.8E+06	4.8E-02	1.00	3	49.0 (87)	5.7 (3.8)
C4	8.8E+05	9.5E-02	2.30	5	51 (122)	4.0 (1.8)
C3	1.4E+06	8.3E-02	2.01	5	53 (128)	3.8 (2.1)
C2	2.6E+06	6.8E-02	1.63	3	53.1 (114)	4.7 (1.9)
C1nobl	8.8E+06	4.1E-02	1.00	0	40.8 (89)	2.9 (1.5)
4nobl	7.3E+05	8.9E-02	2.15	-	60.4 (93)	5.5 (3.4)
C3nobl	1.1E+06	7.7E-02	1.86	-	52.2 (86)	5.9 (2.8)
C2nobl	2.0E+06	6.2E-02	1.50	-	42.5 (81)	5.4 (1.8)
C1nobl	8.8E+06	4.1E-02	1.00	-	40.8 (89)	2.9 (1.5)

Grid sets were defined such that refinement diffusion doubled when grid spacing was halved. The domain refinements in the near- and far-field are varied for grid sets A and B. The balance favours refinement in the far-field for grid set A and refinement at the ship for grid set B, meaning that for similar cell counts, the cell size at the ship hull is larger for set A than for set B (see Figure 2). Grid set C was defined with particular interest for the influence of refinement diffusion on the uncertainty for lateral force. Compared with sets A and B, the refinement diffusion is increased at twice the rate, while the cells at the hull were elongated to an aspect ratio of four to manage the size of the computational grids. The dx reported for grid C is the average of the cell dimensions at the hull. Finally, a subset of grid set C was defined that does not contain boundary layer cells. For grid set Cnobl, not shown in Figure 2, the fitting for diffusion rate vs. cell size h_{vol} returns s_h=-2.06.

A further complication is the inclusion of boundary layer cells at the hull, which will vary in number according to size of the Eulerian mesh, dx, and physical modelling requirement for the cell height adjacent to the hull. For log-law wall modelling, the first cell height is defined to maintain $30 < Y^+ < 100$ in so far as possible. Due to the recirculation region near the transom, Y^+ values smaller than 15 were present for approximately 1.5% of the hull wetted surface. The maximum Y^+ along the leading bilge was considered to be the driving consideration, as separation is expected at that location. Simulations are carried out at model scale, with a relatively low Reynold's number of 2.3×10^6, and the requirements of the log-law wall model were quickly satisfied with increasing grid refinement. By relaxing the requirements for the log-law model, it was possible to define a grid subset without boundary

layer cells. For grid C2nobl, the compromise between cell height metrics $[dx, h_{vol}]$ and refinement diffusion is apparent in the initial cell height, which is smaller than desired for Y^+. Details of grid construction are given in Table 1.

2.3 Simulation Method

The simulation method for the production runs is designed for the assessment of hull geometry variants of the Delft Wind-Assist Series. Considering the volume of work, to be done at full scale, a premium must be placed on economical simulations. Simulation verification is performed at model scale for the purposes of the validation as described in Part 1 of this publication. The validation statement and the extents of the range for modelling error, made out of necessity at model scale, is not directly transferable to full scale simulations. Whereas the Reynolds number for the verification and validation exercise was 2.3E6, full scale simulations are performed for a Reynolds number of 8.3E8. This difference of approximately 3 orders of magnitude means that the turbulence model will have to model a larger range of flow scales, which is presumably detrimental for the modelling error. Still, the ability to perform simulations at full scale is considered desirable; in particular, the ability to reproduce the full-scale boundary layer.

The setup of the computational domain, boundary conditions, and the drift sweep procedure, which are identical for the verification and validation exercise and for the full-scale production runs, will be described here. The meshing strategy for validation runs is described under Results in Section 3.3.

Table 2 FINE/Marine settings

Property	Setting
Flow model	URANS
Turbulence model	EASM
Momentum	ALVSMART
Turbulence	ALVSMART
Multi-fluid	BRICS

The RANS equations are solved with the ISIS-CFD flow solver, developed at Ecole Centrale Nantes. The ISIS-CFD flow solver is an incompressible unsteady RANS method. The unstructured spatial discretization for the transport equations is based on the finite volume method. Free-surface flows are simulated with a conservation equation for the mass fraction. A detailed description of the solver is provided in (Deng, et al., 2005) (Deng, et al., 2006) (Duvigneau & Visonneau, 2003) (Queutey & Visonneau, 2007). Though the unsteady components of the vessel sailing response are not of interest the context of this study, the flow condition is essentially unsteady, and an unsteady-RANS simulation (URANS) is performed. The Explicit Algebraic Stress Model (EASM) is selected as turbulence model to attempt a balance between a Boussinesq-type modelling and more elaborate modelling of Reynolds

stresses,. This $k-\omega$ variant includes modeling for anisotropic turbulence, which is understood to play a key role for the sailing performance of the ship hull, while remaining viable within the scope of work and the available computational resources. The evaluation of convective terms in the momentum equation and the turbulent stresses is performed with the ALVSMART scheme, a blended upwind/central scheme based on the local Courant number (Numeca Int, n.d.). The solution for the free surface is determined following the volume of fluid method, using the BRICS algorithm (Numeca Int, n.d.) that is likewise dependent on the local Courant number. A summary of computation settings is provided in Table 2.

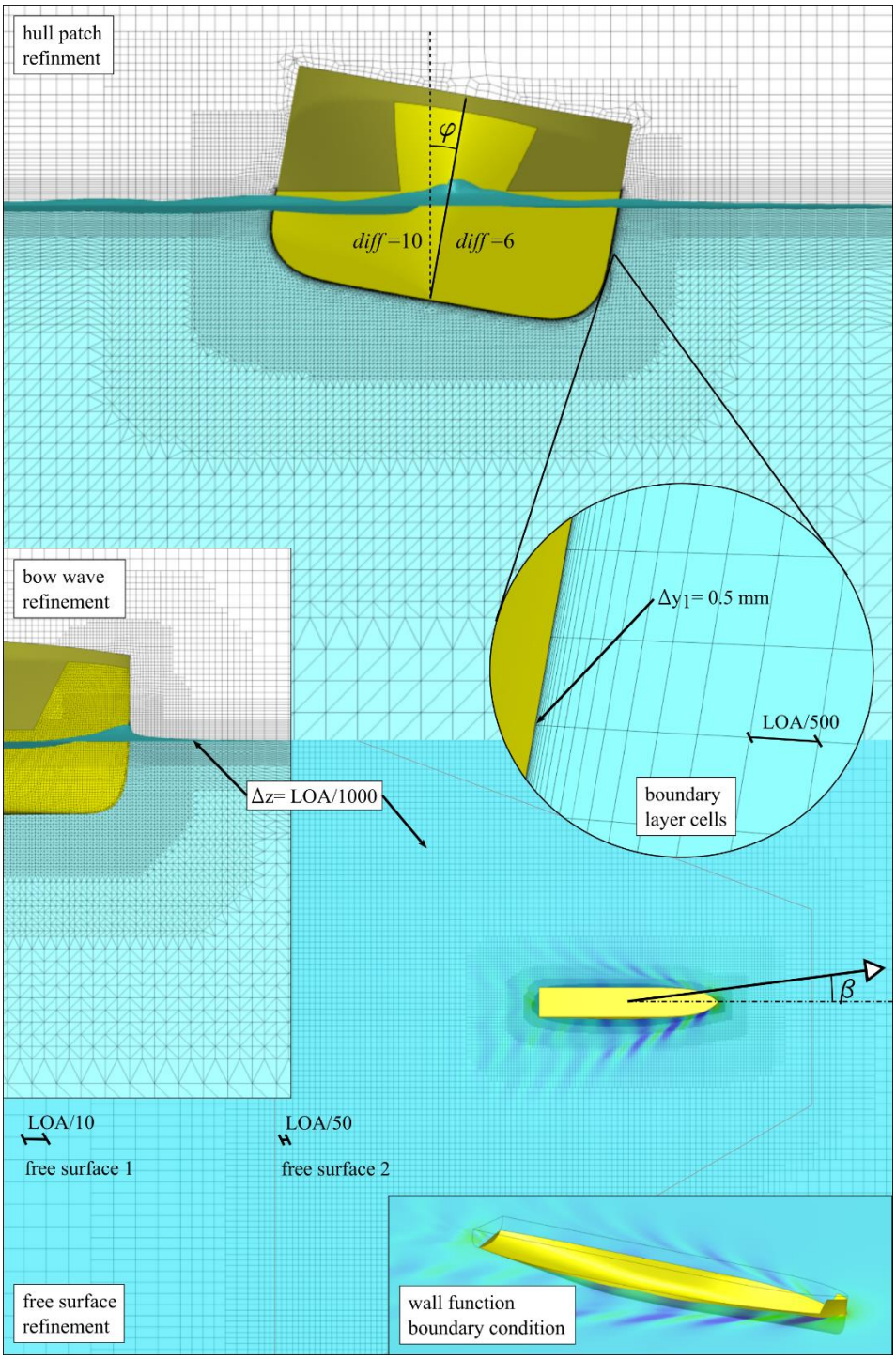


Figure 3 Boundary conditions and mesh details

Domain construction, boundary conditions, and meshing for the free surface are indicated in Figure 3. A logarithmic wall model boundary condition is applied to the ship hull, though it is understood that the correct prediction of separation strength and location is critical for correct modelling some components of the transverse force, and that a logarithmic wall model is essentially unfit for this task. However, the increase in cell count for a wall-resolved simulation (no-slip boundary condition) is not realistic for the routine evaluation of hull variants. Besides controlling the total cell count and simulation computational cost, the logarithmic law boundary condition resolves potential issues with the contact line problem. Finally, the first-cell height requirement of a wall-resolved simulation that includes the free surface for full scale Reynolds numbers may lead to stability issues for the flow solver.

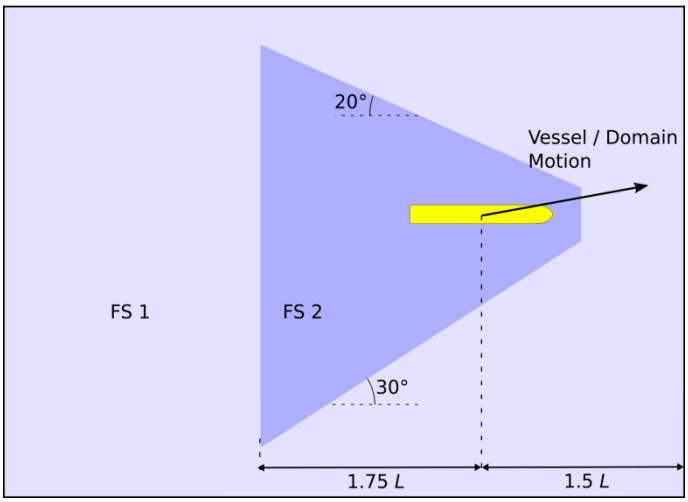


Figure 4 Computational domain for simulation. Note the skewed wedge for the wake refinement zone.

The Drift Sweep procedure (Toxopeus, 2011) was adopted for the efficient analysis of a series of leeway angles and speeds. The domain is meshed once, with the ship aligned with the x-axis, and assigned a prescribed motion (including a leeway angle) within a quiescent fluid, as in Figure 5. Simulation cases proceed from a converged solution to the next combination of leeway angle and vessel speed using a gradual transition, such that the time required for the convergence of the new solution is reduced compared with reinitializing the computation. A coarse time step corresponding to a Courant number of approximately 100 is adopted during this stage to accelerate the convergence of the flow field. The time step is reduced in the final stage to the target Courant number, and integrated fluid forces on the ship hull are determined in the coordinate system aligned with the direction of forward motion. Vessel response may be unsteady due to shedding behaviour around the hull, but only averaged forces are of interest within the context of this study. Integrated fluid forces on the hull are averaged over one characteristic time interval, equal to L/U. The standard deviation for averaged quantities is returned as a measure of the convergence of the simulation to the steady-state solution.

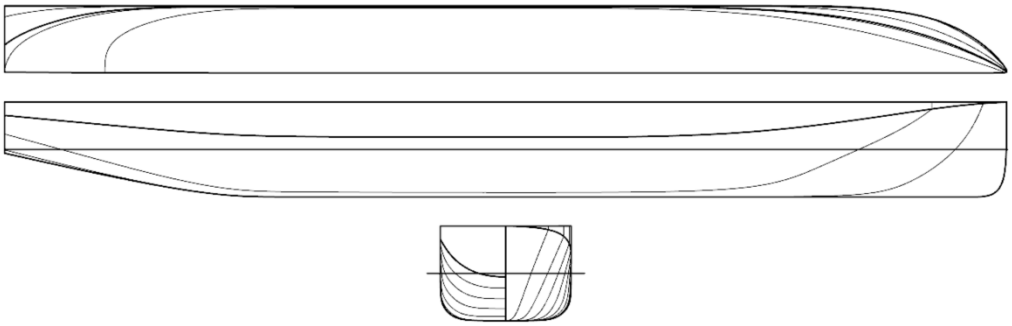


Figure 5 Lines plan for verification case.

Table 3 Main particulars for verification case.

	Full Scale	**Model Scale (α = 50)**
Reynolds Number	8.28×10^8	2.33×10^6
LOA	138 m	2.76 m
Beam	18 m	0.36 m
Draft	6.5 m	0.13 m
Displacement	11896 ton	92.8 kg
C_P	0.719	0.719
C_P	0.764	0.764
C_M	0.942	0.942
LCB	50.13 %	50.13 %
Wetted Surface	3293 m^2	1.312 m^2

The parent hull of the Delft Wind-Assist Series is used for this verification exercise. The lines plan for the bare hull is given in Figure 6 and the main particulars are given in Table 3. The verification exercise is performed at model scale, with a Froude number equal to 0.168, equivalent to 12 knots at full scale. The Reynolds number for simulations is 2.33×10^6. Integrated fluid forces on the model are determined in the coordinate system aligned with the direction of forward motion: resistance X, sideforce Y, and yaw moment N. The sample interval for the verification exercise was $2\ L/U$.

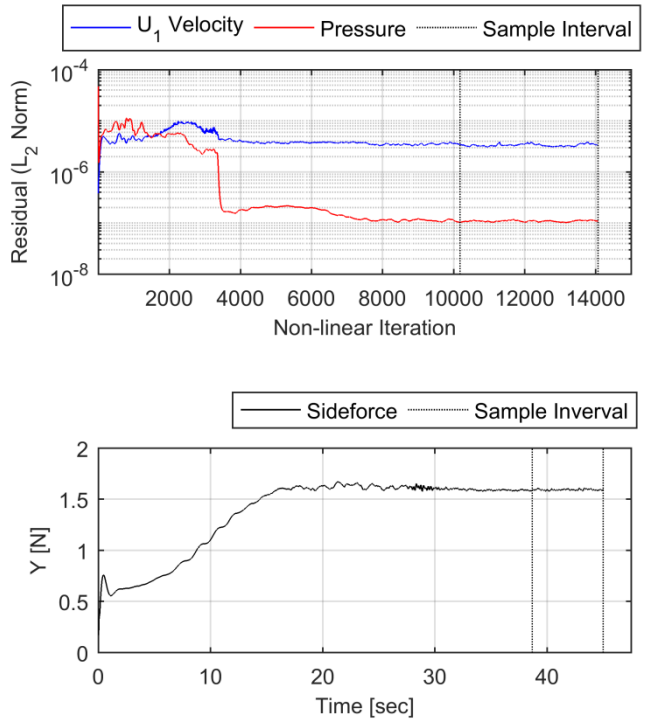


Figure 6 Simulation convergence for a verification case. The sample interval equal to two characteristic time intervals is indicated.

Simulation convergence for the simulation residuals for the U_1 velocity component and the pressure P are reported as:

$$L_2 = \sqrt{\frac{\sum_{i=1}^{N_P}(|\Delta\phi_i|)^2}{N_P}} \qquad (14)$$

Where $\Delta\phi_i$ is the normalized residual, a measure of the change in the flow quantity ϕ between time steps. For the verification exercise, the integrated forces on the ship are the quantities of interest. They are averaged over a sample interval equal to two characteristic time intervals $2*L/U$, as in Figure 7. The standard deviation for these quantities is reported as a metric for simulation convergence to the steady solution that is of interest. The contribution of statistical errors associated with averaging of unsteady phenomena is neglected.

Table 4 Simulation residuals and convergence behaviour.

Grid ID	U_1 Residual (L_2 Norm.)	Pressure Residual (L_2 Norm.)	σ_X	σ_Y	σ_N
A4	3.38E-06	1.69E-07	0.09%	0.51%	0.88%
A3	2.44E-06	1.06E-07	0.15%	0.33%	0.48%
A2	3.34E-06	1.10E-07	0.15%	0.49%	0.69%
A1	2.93E-06	8.75E-08	0.32%	1.24%	1.58%
B4	3.51E-06	1.01E-07	0.05%	0.27%	0.37%
B3	5.24E-06	1.20E-07	0.07%	0.62%	0.56%
B2	3.25E-06	1.28E-07	0.16%	0.93%	1.14%
B1	2.79E-06	1.41E-07	0.23%	1.16%	1.27%
C4	1.68E-06	9.51E-10	0.11%	0.44%	0.65%
C3	4.21E-06	3.40E-08	0.05%	0.40%	0.98%
C2	1.34E-06	1.40E-08	0.08%	0.28%	0.40%
C1nobl	9.62E-08	1.81E-09	0.29%	1.38%	2.23%
C4nobl	1.58E-06	4.08E-07	0.12%	0.31%	0.32%
C3nobl	8.26E-07	2.24E-10	0.07%	0.44%	0.44%
C2nobl	6.49E-08	1.54E-10	0.10%	0.35%	0.52%
C1nobl	9.62E-08	1.81E-09	0.29%	1.38%	2.23%

The simulation residuals are reduced to at least 10^{-5} for all cases. The contribution of iterative errors to the numerical uncertainty, as in Equation 1, is assumed to be negligible.

2.4 Courant Number Study

In the aforementioned procedure, the time step is scaled together with the grid cell size, maintaining a constant Courant number and a consistency for the numerical method for the grid set. The discretization uncertainty obtained with the procedure includes the effect of space and time discretization. However, it is desired to inform the choice of time step for validation runs and production runs, as the blending/switching of discretisation schemes and the interface compression algorithm are functions of the local Courant number. The influence of the choice of time step is investigated with a series of simulations for varying time step. Courant values between 0.25 and 50 were achieved, based on cell refinement at the hull, away from the free surface.

Table 5 Details of Courant number study.

Courant (target)	**Courant (realized)**		
	Grid A2	**Grid B1**	**Grid B3**
0.25	0.24	-	-
0.5	0.49	-	0.36
1	0.98	1.17	1.09
4	2.97	4.64	4.30
16	-	18.41	16.99
50	-	54.06	-

The target Courant number for validation and production runs is selected based on systematic variations in the Courant number performed on three grids, A2, B1, and B3. Simulations for variations in Courant number were performed at 6° leeway. Details for the Courant number study are presented in Table 5.

3 RESULTS FOR NUMERICAL UNCERTAINTY

The simulation verification exercise is performed for the forces integrated over the ship hull: resistance X, sideforce Y, and yaw moment N. In the following, the calculation of the simulation discretisation uncertainty U_D will be discussed for each component. Also, the results for the Courant number study are presented. Finally, the meshing strategy, grid spacing, and target Courant number are defined for validation simulations.

3.1 Numerical uncertainty

The numerical uncertainty is calculated according to the method of Eça and Hoekstra for the discretisation uncertainty, which includes the influence of errors due to spatial and temporal discretisation,. The time step is scaled together with the grid spacing to maintain a constant Courant number and a consistent numerical method. Simulation for grid set A were performed at 0° and 6° leeway. Simulations for grid set B was performed at 6° leeway. Simulations for grid set C and Cnobl were performed at 0° and 9°. All simulations for discretization uncertainty were performed for (target) Courant number equal to four.

For each component: X, Y, and N, the following calculation details are reported: the convergence ratio R, p_{Obs}, the fit selected by the uncertainty procedure, the ratio $\sigma_{fit}/\Delta_{\phi}$, the factor of safety applied, the Richardson extrapolated value ϕ_0, and the uncertainty $U_{h_{Vol}\approx 0.07}$ for each grid set, where all four grid sets overlap (see Table 1). This corresponds to a cell count of approximately 2E6, or grids A4, B4, and C2. Finally, uncertainties computed for each component, on all grids are provided in Table 9.

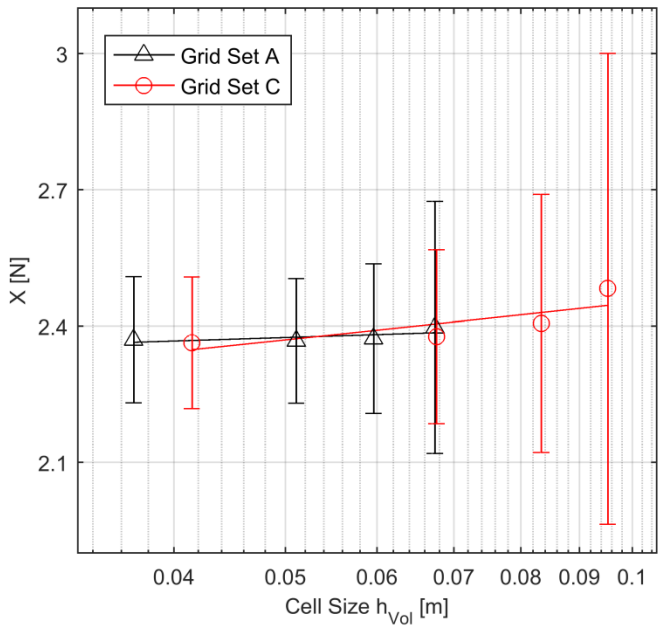


Figure 7 Resistance convergence for grid discretization ($\beta = 0°$). U_D indicated with error bars.

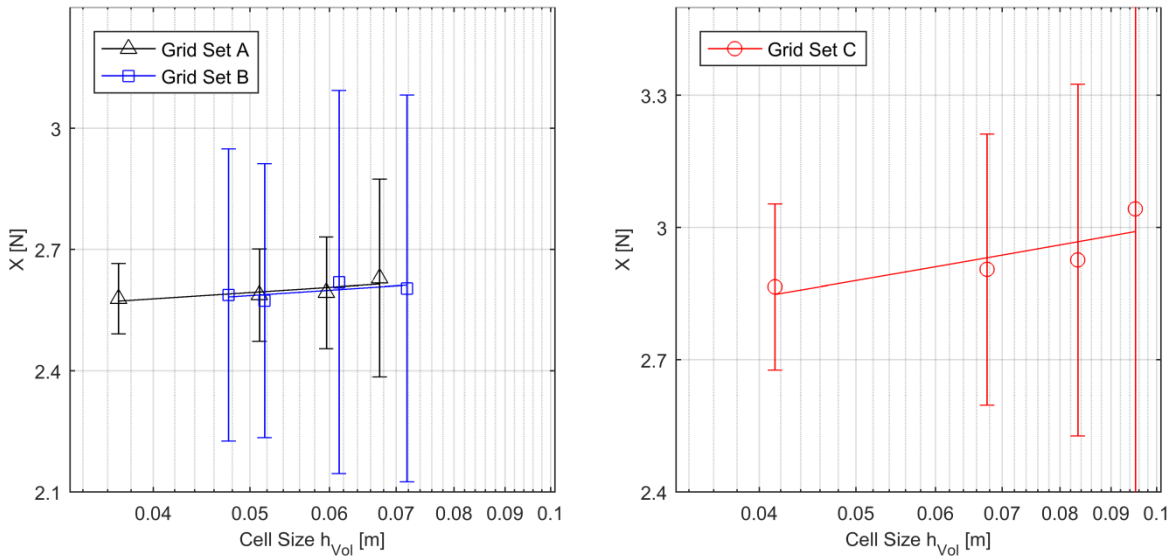


Figure 8 Resistance convergence for grid discretization (left: $\boldsymbol{\beta = 6°}$, right: $\boldsymbol{\beta = 9°}$). $\boldsymbol{U_D}$ indicated with error bars.

Table 6 Calculation details for grid uncertainty estimate for resistance.

Grid Set	$\boldsymbol{R}$	$\boldsymbol{p_{obs}}$	**Fit**	$\boldsymbol{\sigma_{fit}/\Delta_\phi}$	$\boldsymbol{F_S}$	$\boldsymbol{\phi_0}$	$\boldsymbol{U_{h_{Vol}\approx 0.07}}$
A ($\boldsymbol{\beta = 0°}$)	-0.53	17.7	δ_2	1.44	3	2.36	12%
C ($\boldsymbol{\beta = 0°}$)	0.44	7.43	δ_2	0.88	3	2.33	8.1%
A ($\boldsymbol{\beta = 6°}$)	1.56	9.29	δ_2	0.92	3	2.56	9.3%
B ($\boldsymbol{\beta = 6°}$)	-0.30	1.30	δ_{RE}	1.10	3	2.54	18%
C ($\boldsymbol{\beta = 9°}$)	1.85	6.78	δ_2	0.79	3	2.82	11%

The results for discretisation uncertainty for $\beta = 0°$ appear to be congruent (Figure 9). The observed order of convergence is greater than the upper-bound prescribed by Eça and Hoekstra, so that a safety factor of three is applied for both cases. A similar, high observed order of convergence for resistance has been reported by Eça and Hoekstra (Eça & Hoekstra, 2008). The method switches to the second-order fit. The Richardson extrapolated values for these grid sets show excellent agreement for all leeway angles tested. For leeway angle $\beta = 6°$, the meshing approach taken for grid set A is apparently superior, returning approximately half the uncertainty as grid set B, even as the δ_{RE} fitting is used in the uncertainty procedure for grid set B. On the other hand, the convergence ratio R is less than one for grid set B, indicating oscillatory convergence, leading to σ_{fit}/Δ_ϕ>1 and a safety factor of 3.

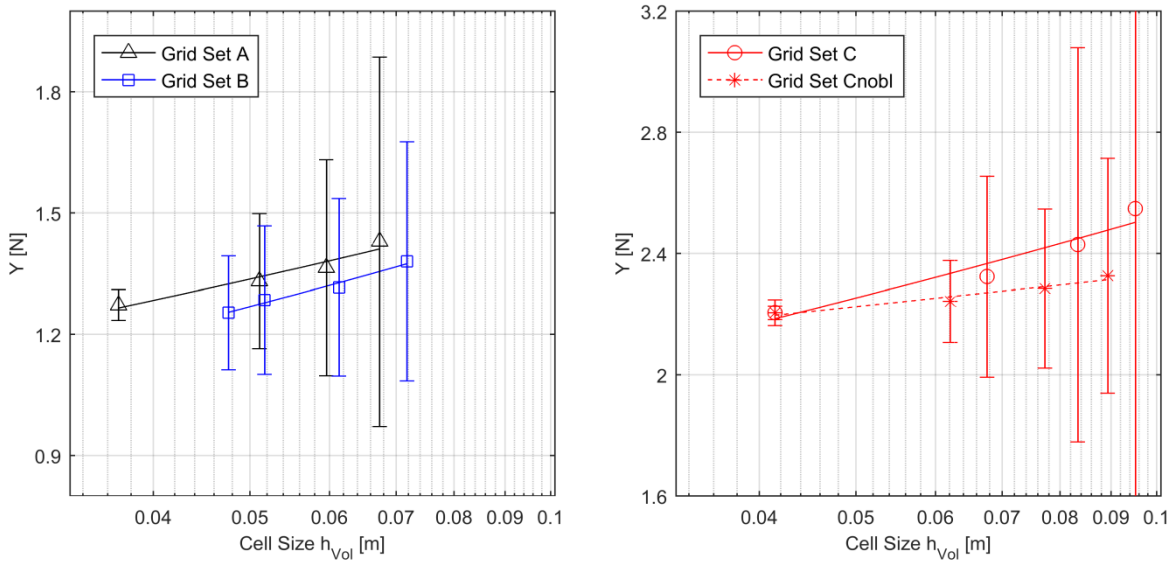


Figure 9 Sideforce convergence for grid discretization (left: $\boldsymbol{\beta = 6°}$, right: $\boldsymbol{\beta = 9°}$). $\boldsymbol{U_D}$ indicated with error bars.

Table 7 Calculation details for grid uncertainty estimate for sideforce.

Grid Set	R	p_{obs}	Fit	σ_{fit}/Δ_ϕ	F_S	ϕ_0	$U_{h_{Vol}\approx 0.7}$
A $(\beta = 6°)$	1.81	2.72	δ_{12}	0.19	3	1.27	32%
B $(\beta = 6°)$	1.0	1.66	δ_{RE}	0.29	1.25	1.15	21%
C $(\beta = 9°)$	1.13	2.55	δ_{12}	0.06	3	2.22	14%
Cnobl $(\beta = 9°)$	0.88	2.38	δ_{12}	0.01	3	2.20	6.0%

The uncertainty estimation for sideforce is compelling. The value of p_{Obs} and the ratio σ_{fit}/Δ_ϕ indicates that confidence is placed on these. Grid set B, where resolution of the ship is favoured, has an observed order of convergence that is in accordance with the interval specified by Eça and Hoekstra. An 11.8% difference between the ϕ_0 value for grid set A and B is observed. The discrepancy may be a product of the differing fits δ_{12} and δ_{RE}. This

discrepancy underscores the substantial grid uncertainty for sideforce. Still, the largest grids A1 and C1nobl have an uncertainty of approximately 3%.

Grid set Cnobl, constructed without boundary layer cells, return the smallest uncertainties (see Figure 10). Calculation details indicate that the quality of the fit and the degree of confidence in the uncertainty assessment are superior to that of grid set C. Grid set C and Cnobl are otherwise identical. In fact the grid quality for Cnobl is detrimentally impacted by the absence of boundary layer cells as seen in Figure 3. The boundary layer cells of grid set C have disrupted geometric similitude, and while the physical modelling (inconsistent Y^+ spacing) and numerical properties (non-orthogonal cells near to the wall) have both been compromised, grid set Cnobl returns superior calculation metrics and lower uncertainties. This is interpreted as the influence of geometric similitude on the uncertainty assessment methods, suggesting that the uncertainties returned following the methodologies in this paper may be overstated.

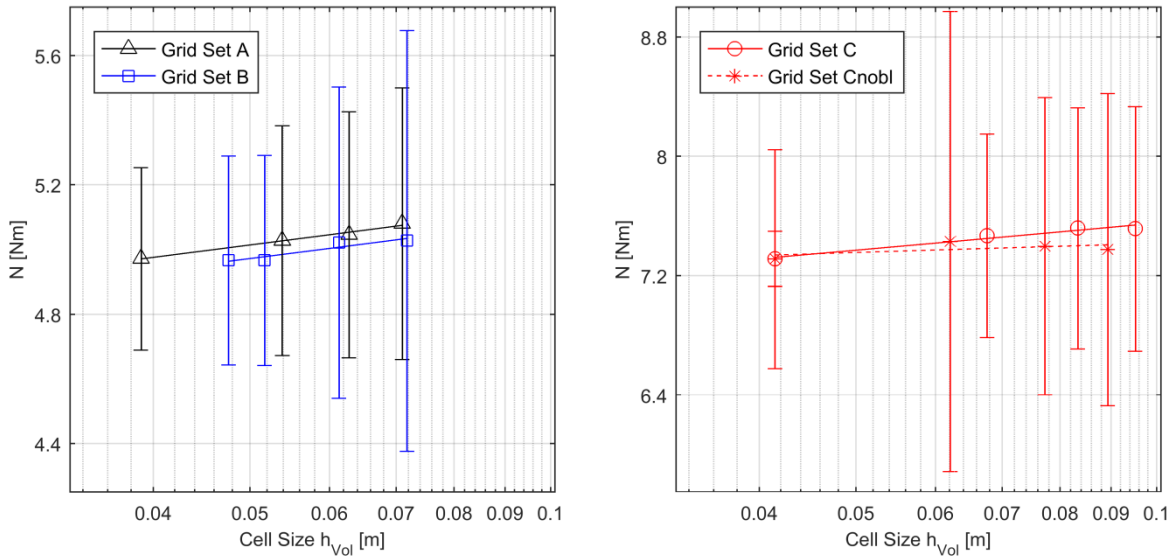


Figure 10 Yaw moment convergence (left: $\boldsymbol{\beta = 6°}$, right: $\boldsymbol{\beta = 9°}$). $\boldsymbol{U_D}$ indicated with error bars.

Table 8 Calculation details for discretisation uncertainty estimate for yaw moment.

Grid Set	R	p_{obs}	Fit	σ_{fit}/Δ_ϕ	F_S	ϕ_0	$U_{h_{Vol}\approx 0.7}$
A ($\beta = 6°$)	3.06	0.65	δ_{RE}	0.21	1.25	4.75	8.3%
B ($\beta = 6°$)	0.00	3.22	δ_2	0.34	3	4.83	13%
C ($\beta = 9°$)	3.14	3.10	δ_2	0.99	3	7.21	9.1%
Cnobl ($\beta = 9°$)	-3.59	2.78	δ_2	2.04	3	7.32	22%

The procedure for the grid uncertainty of the yaw moment is very well behaved for grid set A. For other grid sets the convergence behaviour is such that the safety factor is increased to three and a second-order fit is applied. Results from grids C and Cnobl are poorly

fit, as indicated by $\sigma_{fit}/\Delta_{\phi}$. In particular, C2nobl, which exhibits oscillatory convergence, and where the large difference for the term $(\phi_i - \phi_{fit})$ from Equation 12 results in large uncertainties (see Figure 11). The Richardson extrapolation value for zero-grid spacing differs by 8% for grid C and Cnobl. The values for zero-grid spacing of grid sets A and B lie within 3% of each-other.

Table 9 Complete results for numerical uncertainty.

Grid ID	h_{vol}	U_{Num}: X	U_{Num}: Y	U_{Num}: N
$\beta = 0^{\circ}$				
A4	6.7E-02	0.28 N (12%)	-	-
A3	6.0E-02	0.16 N (6.9%)	-	-
A2	5.1E-02	0.14 N (5.8%)	-	-
A1	3.7E-02	0.14 N (5.9%)	-	-
C4	9.5E-02	0.52 N (21%)	-	-
C3	8.3E-02	0.28 N (12%)	-	-
C2	6.8E-02	0.19 N (8.1%)	-	-
C1nobl	4.1E-02	0.14 N (6.1%)	-	-
$\beta = 6^{\circ}$				
A4	7.1E-02	0.24 N (9.3%)	0.46 N (32%)	0.42 Nm (8.3%)
A3	6.3E-02	0.14 N (5.3%)	0.27 N (20%)	0.38 Nm (7.5%)
A2	5.4E-02	0.11 N (4.4%)	0.17 N (13%)	0.36 Nm (7.1%)
A1	3.9E-02	0.09 N (3.4%)	0.04 N (3.0%)	0.28 Nm (5.7%)
B4	7.2E-02	0.48 N (18%)	0.30 N (21%)	0.65 Nm (13%)
B3	6.1E-02	0.47 N (18%)	0.22 N (17%)	0.48 Nm (10%)
B2	5.2E-02	0.34 N (13%)	0.18 N (14%)	0.32 Nm (6.5%)
B1	4.8E-02	0.36 N (14%)	0.14 N (11%)	0.32 Nm (6.5%)
$\beta = 9^{\circ}$				
C4	9.5E-02	0.75 N (25%)	1.00 N (39%)	0.82 Nm (11%)
C3	8.3E-02	0.40 N (14%)	0.65 N (27%)	0.81 Nm (11%)
C2	6.8E-02	0.31 N (11%)	0.33 N (14%)	0.68 Nm (9.1%)
C1nobl	4.1E-02	0.19 N (6.6%)	0.04 N (1.9%)	0.19 Nm (2.5%)
C4nobl	8.9E-02	-	0.39 N (17%)	1.04 Nm (22%)
C3nobl	7.7E-02	-	0.26 N (11%)	1.00 Nm (20%)
C2nobl	6.2E-02	-	0.13 N (6.0%)	1.54 Nm (22%)
C1nobl	4.1E-02	-	0.02 N (1.0%)	0.73 Nm (9.3%)

The results presented above can be better interpreted by recalling the grid set definition in terms of the cell size dx and the refinement diffusion (see Figure 2). First, the large uncertainty values reported for grid set B are interesting as the cell size dx for grids B1-B3 is

smaller than the cell size dx for Grid A2. On the other hand, the two largest grids, A1 and C1nobl, where quite small uncertainties are computed for all force components, have the largest refinement diffusion. This is interpreted as a consequence of proper resolution of the wake of shed vorticity associated with sideforce production. For the grid definition for validation simulations, the refinement diffusion parameter should be prioritised over cell size dx. The general trend for the poor performance of grid set B does not hold for the uncertainty for sideforce U_{Num}: Y. For grids A2-A4 and B2-B4, where the refinement diffusion varies uniformly, one can observe the influence of the cell size dx on the sideforce uncertainty, which increases quickly for grid set A after grid A2 (cell size dx=0.006 (≈L/500).

3.2 Courant Number Study

Time-discretisation uncertainties are determined for three grids, A2, B1, and B3, following the same procedure as above. The temporal uncertainty corresponding to a target Courant number of four is reported. This is the same target Courant number used for the discretisation uncertainty calculations presented above.

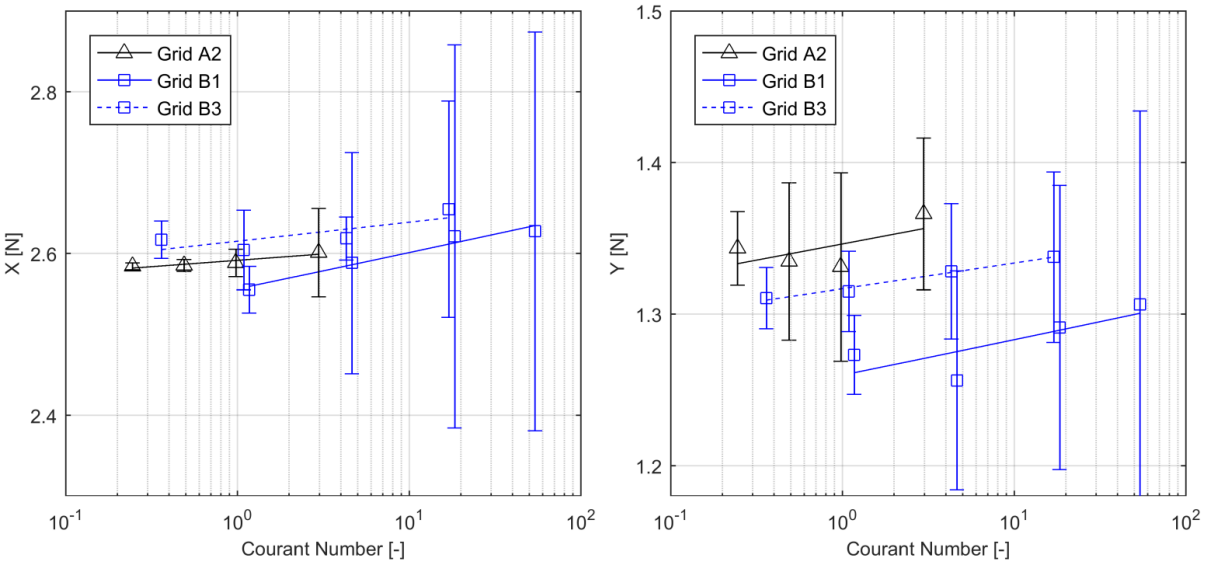


Figure 11 Resistance convergence for Courant number variation. ($\boldsymbol{\beta = 6°}$) $\boldsymbol{U_T}$ indicated with error bars.

Figure 12 Sideforce convergence for Courant number variation ($\boldsymbol{\beta = 6°}$). $\boldsymbol{U_T}$ indicated with error bars.

Table 10 Calculation details for Courant number parameter study for resistance.

Grid	R	p_{obs}	Fit	σ_{fit}/Δ_ϕ	F_S	ϕ_0	$U_{Co\approx4}$
A2	0.30	1.15	δ_{RE}	0.05	1.25	2.58	2.1%
B1	1.0	0.53	δ_{RE}	0.67	1.25	2.52	9.0%
B3	-0.89	2.33	δ_2	0.64	3	2.61	1.0%

Calculation details for grids A2, B1, and B3 indicate that confidence is placed in the time uncertainty estimates (see Table 10). The Richardson extrapolations for zero-time step and zero grid spacing show close agreements. The ϕ_0 value for grid A2 and B1 differ by 2.3%. Finally, the ϕ_0 values for zero time step and zero grid spacing for grid sets A and B differ by less than 1% each. A marked increase in the uncertainty estimate is observed for the set of large Courant numbers, performed with grid set B1.

Table 11 Calculation details for Courant number parameter study for sideforce.

Grid	R	p_{obs}	**Fit**	σ_{fit}/Δ_ϕ	F_S	ϕ_0	$U_{Co=4}$
A2	2.44	19.97	δ_{12}	0.22	3	1.35	3.7%
B1	-0.48	1.55	δ_{RE}	0.90	1.25	1.27	5.8%
B3	0.33	0.29	δ_{12}	0.05	3	1.31	3.3%

Courant number variation on grid B1 returns an observed order of convergence equal to 1.55 and σ_{fit}/Δ_ϕ less than one, yet the uncertainty $U_{Co=4}$ is the largest calculated. By contrast, grids A2 and B3 returned an observed order of convergence outside the range prescribed by Eça and Hoekstra and switch to the mixed order fit δ_{12} with safety factor equal to three. The ϕ_0 value for grids A2 and B3 differ from ϕ_0 value of grid B1 by 5.9% and 3.1% respectively, which is in accordance with the presence of considerable discretisation uncertainty calculated for sideforce on these grids (for A2: U_D=13%, B1: U_D=14%, B3: U_D=17%). Finally, the ϕ_0 value for zero-time step for grid A2 differs from the ϕ_0 value for zero grid spacing for grid set A by 6.3%, while the extrapolated values for zero time step for grid B1 and zero grid spacing for grid set B differ by 10%.

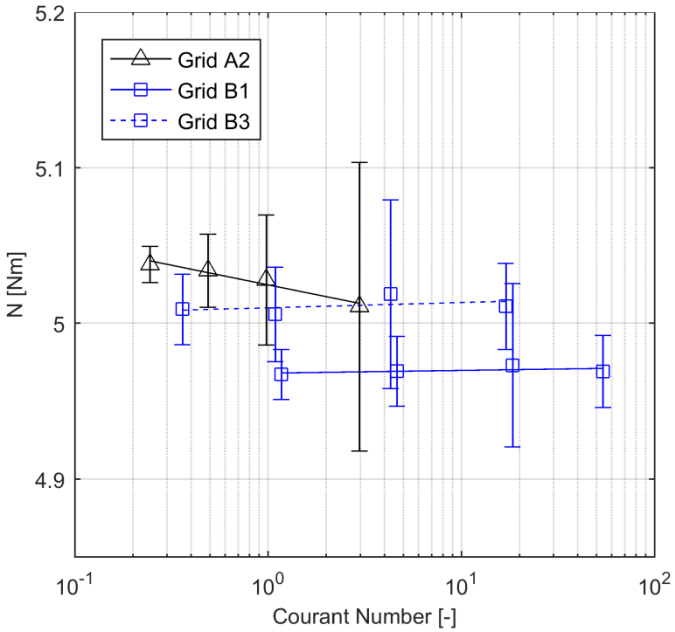


Figure 13 Yaw moment convergence behaviour for Courant number variation ($\boldsymbol{\beta = 6}$°). $\boldsymbol{U_T}$ indicated with error bars.

Table 12 Calculation details for time step uncertainty estimate for yaw moment.

Grid	R	p_{obs}	Fit	σ_{fit}/Δ_ϕ	F_S	ϕ_0	$U_{Co=4}$
A2	0.64	-	δ_{12}	0.13	3	5.04	1.8%
B1	0.53	-	δ_{12}	0.15	3	4.97	0.4%
B3	-0.25	-	δ_{12}	1.03	3	5.01	1.2%

The value for yaw moment varies very little with Courant number, and the time discretization uncertainty is insignificant. Extrapolations for zero-time step lie within 1% of each other and within 6% of the extrapolated zero-grid size value. The fitting for the observed order of convergence does not succeed. The method of Eça and Hoekstra returns the safety factor of three with very small values for σ_{fit}/Δ_ϕ, except for grid B3, where oscillatory convergence is observed.

Table 13 Complete results for Courant number study.

Courant (target)	Mean	Grid A2	Grid B1	Grid B3
	$\boldsymbol{U_T}$: $\boldsymbol{X}$	(U_D=4.4%)	(U_D=14%)	(U_D=18%)
50	0.25 N (9.4%)	-	0.25 N (9.4%)	-
16	0.19 N (7.0%)	-	0.24 N (9.0%)	0.13 N (5.0%)
4	0.07 N (2.8%)	0.05 N (2.1%)	0.14 N (5.3%)	0.03 N (1.0%)
1	0.03 N (1.2%)	0.02 N (0.7%)	0.03 N (1.1%)	0.05 N (1.9%)
0.5	0.02 N (0.6%)	0.01 N (0.3%)	-	0.02 N (0.9%)
0.25	0.00 N (0.2%)	0.00 N (0.2%)	-	-
	$\boldsymbol{U_T}$: $\boldsymbol{Y}$	(U_D=13%)	(U_D=11%)	(U_D=17%)
50	0.13 N (9.8%)	-	0.13 N (9.8%)	-
16	0.07 N (5.7%)	-	0.04 N (7.3%)	0.06 N (4.2%)
4	0.06 N (4.3%)	0.05 N (3.7%)	0.07 N (5.8%)	0.04 N (3.3%)
1	0.04 N (2.9%)	0.06 N (4.7%)	0.03 N (2.1%)	0.03 N (2.0%)
0.5	0.04 N (2.7%)	0.05 N (3.9%)	-	0.02 N (1.5%)
0.25	0.02 N (1.8%)	0.02 N (1.8%)	-	-
	$\boldsymbol{U_T}$: $\boldsymbol{N}$	(U_D=7.1%)	(U_D=6.5%)	(U_D=10%)
50	0.02 N (0.5%)	-	0.02 Nm (0.5%)	-
16	0.04 N (0.8%)	-	0.05 Nm (1.1%)	0.03 Nm (0.5%)
4	0.06 N (1.2%)	0.09 Nm (1.8%)	0.02 Nm (0.4%)	0.06 Nm (1.2%)
1	0.03 N (0.6%)	0.04 Nm (0.8%)	0.02 Nm (0.3%)	0.03 Nm (0.6%)
0.5	0.02 N (0.5%)	0.02 Nm (0.5%)	-	0.02 Nm (0.5%)
0.25	0.01 N (0.2%)	0.01 Nm (0.2%)	-	-

The time-discretisation uncertainties obtained by systematically varying the Courant number are averaged at each target Courant number and presented in Table 13 along with the uncertainties determined on each grid. The discretisation uncertainty, which includes the time-uncertainty at $Co = 4$ is provided for context. If an RSS combination for the simulation error is assumed as in Equation 1 (Wilson, et al., 2006):

$$U_D^2 = U_G^2 + U_T^2 \qquad (15)$$

Then the results calculated for U_D and U_T at $Co = 4$ may be used to infer conclusions about the composition of the numerical uncertainty (iterative errors have been neglected throughout this study). The influence of the range of data in relation to the extents of the asymptotic range has been discussed. The increased safety factor for anomalous convergence behaviour reflects the poor confidence placed on the uncertainty estimation. Results for Courant variations on grid A2 are regarded as the most meaningful. For this grid, the contribution of time-discretisation uncertainty is only significant for the resistance, for which U_D=4.4%,

U_G=3.9%, and U_T=2.1%. A target Courant number is determined by linear interpolation of the averaged values for U_T such that the contributions of the spatial and temporal uncertainties to the discretisation uncertainty are equal. This condition is satisfied for Courant number equal to 8.

3.3 Mesh Definition for Validation

A mesh for validation simulation is defined based on the results presented above for simulation verification. The mesh resolution and time step is defined such that the contribution of the numerical uncertainty is commensurate with the other uncertainties in the validation exercise. At the same time, the mesh definition must be computationally affordable considering the volume of simulations planned. The meshing and time step for validation simulations are described.

The following guidelines are adopted for the meshing strategy. The discretisation uncertainty is reduced for grids with larger refinement diffusion, or when the refinement of the domain is prioritised over refinement at the ship. For both cases, this is interpreted as a consequence of the resolution of the wake of the ship. Therefore, the refinement diffusion in the downstream direction is favoured over the upstream direction. Cell size dx corresponding to L/500 is selected following the discussion of results for sideforce uncertainty for grids A2:A4 and B2:B4. Four layers of boundary layer cells are inserted to satisfy modelling requirement for Y^+

Table 14 Numerical uncertainty for simulation validation.

	$\boldsymbol{U_{Num}}$: $\boldsymbol{X}$	$\boldsymbol{U_{Num}}$: $\boldsymbol{Y}$	$\boldsymbol{U_{Num}}$:$\boldsymbol{N}$
$\boldsymbol{\beta = 0^\circ}$	0.14 N	-	-
$\boldsymbol{\beta = 6^\circ}$	0.11 N	0.13 N	0.34 Nm
$\boldsymbol{\beta = 9^\circ}$	0.23 N	0.14 N	0.35 Nm

Estimates for numerical uncertainty for validation simulations are given in Table 14, with a cell size dx=0.0054 and a refinement diffusion equal to 10 in the downstream direction. The corresponding grid size h_{Vol}=0.05, for 6E6 cell count. The numerical uncertainties were approximated by linear interpolation using h_{Vol} and available results on grids sets A and C. The time step is selected to achieve a target Courant number of 8. These values are adopted in Part 1 of this series describing the experimental validation for this simulation methodology.

3.4 Turbulence model and wall treatment

The selection of the EASM turbulence model is motivated by an appreciation for the physics of sideforce production, where anisotropy in the dissipation of shed vorticity is understood to play a key role. This is borne out in comparisons made using the validation data set for simulations with wall function using the k$-\omega$ SST turbulence model and the EASM turbulence model. The result is reported as the comparison error for sideforce, which is given as a percentage of the range of experimental values.

$$E_{\text{Ens}} = (100) * \frac{Sim - Exp}{\frac{1}{2}\left(max(Exp) - min(Exp)\right)} \qquad (16)$$

Further discussion and results for the ensemble comparison error are presented in Part 1.

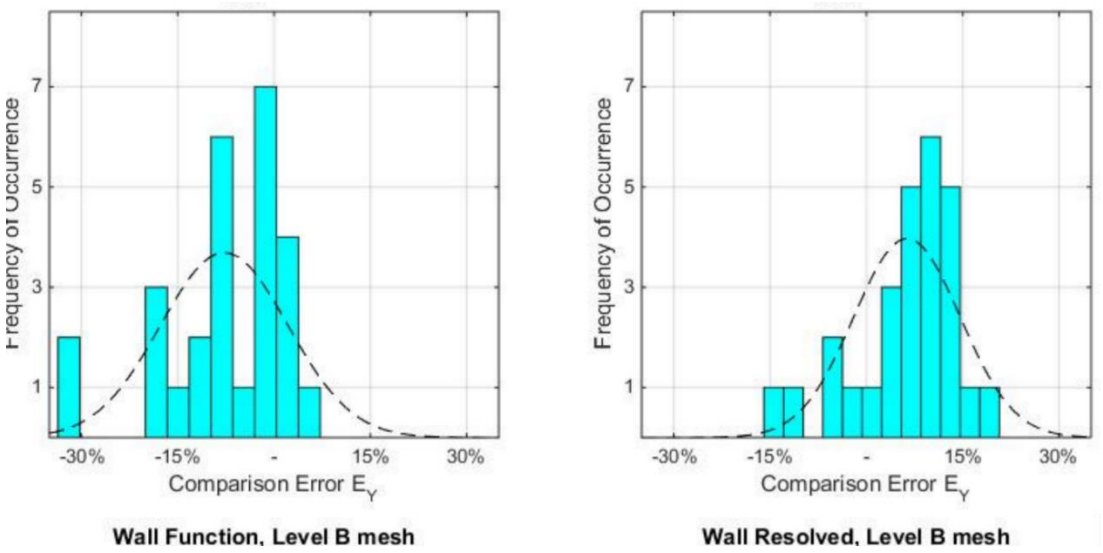


Figure 14 Eens (sideforce) for varying wall-treatments. (n=27).

The comparison error for two wall treatments are plotted as histograms in Figure 14. The errors for each component appear to be normally distributed. The statistics of the distribution are presented in Table including a 95% confidence interval of the ensemble comparison error, which is understood as an estimate for the range of the comparison errors for the Delft Wind-Assist Series. For the sideforce in particular, a -2% mean offset indicates there is a systematic under-prediction by the simulation. The negative outliers in Figure 14 correspond to Hull 16, with sharp bilges, where pronounced separation of bilge vortices is expected. Simulation for sideforce is consistently under-predicted for this hull. For the k-ω SST turbulence model, the sideforce is nearly always under-predicted (this is for hulls \#1, \#16 and \#19). Apparently improving the modeling of anisotropic turbulence with the EASM turbulence model has centered the distribution and reduced the number of outliers.

Table 15 Statistics for distribution of comparison errors

E_{Ens}	$\mu_{\text{Ens}}[\%]$	σ_{Ens} [%]	$CI95_{\text{Ens}}$ [%]
Validation Set			
Resistance X	−0.6	5.0	10.8
Sideforce Y	−2.0	7.5	17.4
Yaw Moment N	0.9	4.2	9.3
Wall Treatments			
$EASM$ (Val. Mesh)	−2.0	7.5	17.4
Wall-resolved $EASM$ (B3)	−2.0	7.5	23.3
Log-law $EASM$ (B3)	−2.0	7.5	28.1
Log-law $k-\omega$ (C2)	−11.3	12.6	32.7

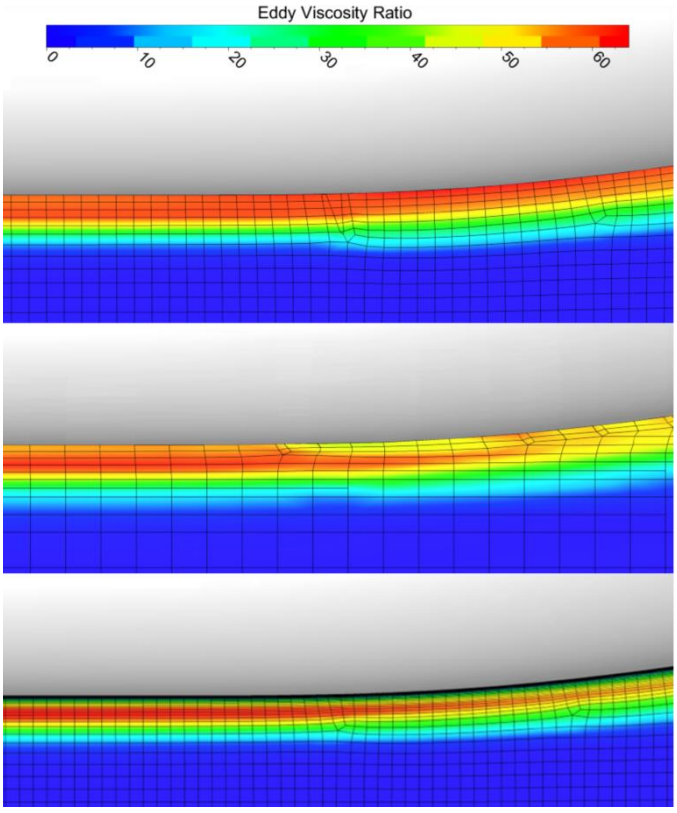


Figure 15 Boundary layer development for grids A3, C2nobl, and a wall-resolved solution (top to bottom). Colour contours indicate eddy viscosity ratio.

The absence of boundary layer cells for grid set Cnobl influences the solution near the wall as seen in Figure 3, where a detail of the hull is shown as the keel line turns from the parallel midbody towards the upward-sloping buttock lines of the pram stern. A cross-section of the computational domain is shown in the x-z plane including cell borders and colour contours for the eddy viscosity ratio. Three solutions are shown: grid A3, with four boundary layer cells (top), grid C2nobl (middle), and a wall-resolved mesh (bottom), where a no-slip boundary condition is imposed at the hull. For this mesh, thirty boundary layer cells are inserted to

achieve a Y^+ less than one. The thickness of the region of eddy viscosity production is similar for all meshes, and lies within the thickness of the boundary layer cell region for grid A3 (top). The reduction in eddy viscosity ratio along the upward sloping keel, observed for the wall-resolved simulation, is less evident for grid A3. Finally, the absence of boundary layer cells for grid Cnobl clearly influences the flow inside the boundary layer, where mesh irregularities were introduced in the snap-to-geometry step during mesh construction. Interestingly, the quality of the data for Richardson extrapolation, as measured by p_{Obs} and the ratio σ_{fit}/Δ_ϕ indicate that greater confidence is placed in the uncertainty estimates based on grid set Cnobl (see Section 3.2). As discussed in Section 2.1, the methods for uncertainty assessment are predicated on geometric similitude, which is better preserved for the grid set without boundary layer cells.

4 CONCLUSION

The numerical uncertainty for RANS CFD simulations for integrated forces for the wind-assist ship hull has been investigated. The verification exercise described herein is a necessary prerequisite for the reliable assessment of wind assist hull-form variants using CFD simulations. This work complements the validation exercise presented in Part 1 of this series describing the simulation method employed in this research. The sailing vessel, operating with a leeway angle to produce hydrodynamic sideforce, will trail a wake of large vortices, the separation and evolution of which is understood to be the principal simulation challenge. This two-part series is an attempt to validate a simulation method that can capture this phenomenon yet remain computationally affordable in light of the volume of simulations anticipated.

The numerical uncertainty has been determined for several grid sets with differing meshing strategies, and for a range of Courant numbers. The objective was to inform the meshing strategy and time step choice for validation and production runs. It was observed that grids with a large refinement diffusion exhibited superior performance as measured by the calculated uncertainties. This is interpreted as a requirement on the refinement of the wake of the sailing vessel. The influence of cell size at the ship hull was most apparent for the sideforce uncertainty. Finally, improvement in geometric similarity for grid set Cnobl, defined without boundary layer cells, gave better-behaved convergence and resulted in lower uncertainty estimates. This implies that the uncertainty estimates for practical meshes (with boundary layer cells) may be overstated. The meshing strategy and time step adopted for validation and production runs was defined. Numerical uncertainty for validation runs as adopted for the validation exercise presented in Part 1 of this paper are presented in Table 14.

ACKNOWLEDGEMENTS

This research is conducted with the support of the European Commission as part of the Joules Project. The author would also like to thank the Vaderland Fonds for their support. Computations were performed at the SARA supercomputer facility as part of sponsorship by NWO Exacte Natuur en Wetenschappen, ENW (NWO Physical Sciences Division).

REFERENCES

ASME, 2009. *Standard for Verification and Validation in Computational Fluid Dynamics and Heat Transfer,* s.l.: ASME.

Celik, B. & Li, J., 2005. Assessment of Numerical Uncertainty for the Calculations of Turbulent Flow over a Backward-facing Step. *Internaional Journal for Numerical Methods in Fluids,* Volume 49, pp. 1015-1031.

Celik, I. & Karatekin, O., 1997. Numerical Experiments on Application of Richardson Extrapolation with Nonuniform Grids. *Journal of Fluids Engineering,* Volume 119, pp. 584-590.

Celik, I., Li, J., Hu, G. & Shaffer, C., 2005. Limitations of Richardson Extrapolation and some Possible Remedies. *Journal of Fluids Engineering,* Volume 127, pp. 795-805.

Coleman, H. & Stern, F., 1997. Uncertainties and CFD Code Validation. *Journal of Fluids Engineering,* pp. 795-803.

Deng, G. B., Guilmineau, E., Queutey, P. & Visonneau, M., 2005. *Ship Flow Simulations with the ISIS CFD Code.* Tokyo, CFD Workship Tokyo.

Deng, G. B., Queutey, P. & Visonneau, M., 2006. *A Code Verificaion Exercise for the Unstructured Finite Volume CFD Solver ISIS-CFD.* Delft, s.n.

Duvigneau, R. & Visonneau, M., 2003. On the role played by turbulence closures in hull shape optimization at model and full scale. *Journal of Marine Science and Technology,* Volume 8, pp. 11-25.

Eça , L. & Hoekstra, M., 2008. The numerical friction line. *Journal of Marine Science and Technology,* 13(4), pp. 328-345.

Eça, L., Guilherme, V. & Hoekstra, M., 2010. Code Verification, Solution Verification, and Validation in RANS Solvers. *Proceedings ASME Conference ence on Ocean, Offshore, and Arctic Engineering.*

Eça, L. & Hoekstra, M., 2014. A Proceedure for the Estimation of the Numerical Uncertainty of CFD Calculations Based on Grid Refinement Studies. *Journal of Computational Physics,* Volume 262, pp. 104-130.

International Towing Tank Commitee, 2008. Uncertainty Analysis in CFD: Verification and Validation, Methodology and Proceedures.

ITTC, 2008. Recommended Practices- Uncertainty Analysis in CFD Verification Proceedures.

Numeca Int, n.d. ISIS Theoretical Manual.

Oberkampf, W. L., 1994. A Proposed Framework for Computational Fluid Dynamics Code Calibration/Validation. *AIAA,* Issue 94-2540.

Pereira, F., Eca, L. & Vaz, G., 2017. Verification and Validation exercizes for the flow around the KVLCC2 tanker at model and full-scale Reynolds numbers. *Ocean Engineering,* Volume 129, pp. 133-148.

Queutey, P. & Visonneau, M., 2007. An interface capturing method for free-surface hydrodynamic flows. *Computers and Fluids,* 36(November), pp. 1481-1510.

Richardson, L., 1927. The Deferred Approach to the Limit. *Transactions of Royal Society London,* Volume 226, pp. 299-361.

Roache, P. J., 1997. Quantification of Uncertainty in Computational Fluid Dynamics. *Ann. Rev. of Fluid Mechanics,* Volume 29, pp. 123-160.

Rosetti, G., Vas, G. . & Fujarra, A., 2012. URANS Calculations for Smooth Circular Cylinder Flow in a Wide Range of Reynolds Numbers: Solution Verification and Validation. *Journal of Fluids Engineering,* 134(December).

Stern, F. et al., 2005. Statistical Approach for Estimating Intervals of Certification or Biases of Facilities or Measurement Systems Including Uncertainties. *ASME Journal of Fluids Engineering,* 127(2), pp. 604-610.

Stern, F., Wilson, R., Coleman, H. . & Paterson, E., 2001. Comprehensive Approach to Verification and Validation of CFD Simulations--Part 1: Methodology and Procedures. *Journal of Fluids Engineering,* pp. 793-810.

Stern, F., Wilson, R. . & Shao, J., 2005. Quantitative V&V of CFD Simulations and Certification of CFD Codes. *International Journal for Numerical Methods in Fluids,* Volume 50, pp. 1335-1355.

Surf SARA, n.d. *Description of the Cartesius system.* [Online]
Available at: https://userinfo.surfsara.nl/systems/cartesius/description

Toxopeus, S. L., 2011. Practical application of viscous-flow calculations for the simulation of manoeuvering ships. *PhD Thesis.*

van der Kolk, N. J., 2016. *Hydrodynamics of Wind-Assisted Ship Propulsion: Modelling of Hydrodynamic Sideforce.* Amsterdam, s.n.

van der Kolk, N. J., Keuning, J. A. & Huijsmans, R. H. M., 2016. *Hydrodynamics of Wind-Assisted Ship Propulsion: Verification of RANS Simulations.* Egmond aan Zee, s.n.

Viola, I. M., Bot, P. & Riotte, M., 2013. On the Uncertainty of CFD in Sail Aerodynamics. *International Journal for Numerical Methods in Fluids,* Volume 72, pp. 1146-1164.

Wilson, R., Carrica, P. & Stern, F., 2006. Unsteady RANS method for ship motions with application to roll for a surface combatant. *Computers and Fluids,* Volume 35, pp. 501-524.